

The role of viscosity on drop impact forces

Vatsal Sanjay^{1†}, Bin Zhang^{2‡}, Cunjing Lv^{2¶}, and Detlef Lohse^{1,3||}

¹Physics of Fluids Group, Max Planck Center for Complex Fluid Dynamics, Department of Science and Technology, and J. M. Burgers Centre for Fluid Dynamics, University of Twente, P. O. Box 217, 7500 AE Enschede, The Netherlands

²Department of Engineering Mechanics, AML, Tsinghua University, Beijing 100084, China

³Max Planck Institute for Dynamics and Self-Organization, Am Fassberg 17, 37077 Göttingen, Germany

(Received xx; revised xx; accepted xx)

A liquid drop impacting a rigid substrate undergoes deformation and spreading due to normal reaction forces, which are counteracted by surface tension. On a non-wetting substrate, the drop subsequently retracts and takes off. Our recent work (Zhang et al., *Phys. Rev. Lett.*, vol. 129, 2022, 104501) revealed two peaks in the temporal evolution of the normal force $F(t)$ —one at impact and another at jump-off. The second peak coincides with a Worthington jet formation, which vanishes at high viscosities due to increased viscous dissipation affecting flow focusing. In this article, using experiments, direct numerical simulations, and scaling arguments, we characterize both the peak amplitude F_1 at impact and the one at take off (F_2) and elucidate their dependency on the control parameters: the Weber number We (dimensionless impact velocity) and the Ohnesorge number Oh (dimensionless viscosity). The first peak amplitude F_1 and the time t_1 to reach it depend on inertial timescales for low viscosity liquids, remaining nearly constant for viscosities up to 100 times that of water. For high viscosity liquids, we balance the rate of change in kinetic energy with viscous dissipation to obtain new scaling laws: $F_1/F_\rho \sim \sqrt{Oh}$ and $t_1/\tau_\rho \sim 1/\sqrt{Oh}$, where F_ρ and τ_ρ are the inertial force and time scales, respectively, which are consistent with our data. The time t_2 at which the amplitude F_2 appears is set by the inertia-capillary timescale τ_γ , independent of both the viscosity and the impact velocity of the drop. However, these properties dictate the magnitude of this amplitude.

Key words:

1. Introduction

Drop impacts have piqued the interest of scientists and artists alike for centuries, with the phenomenon being sketched by da Vinci (1508) in the early 16th and photographed by Worthington (1876a,b) in the late 19th century. It is, indeed, captivating to observe raindrops hitting a solid surface (Kim et al. 2020; Lohse & Villermaux 2020) or ocean spray affecting maritime structures (Berny et al. 2021; Villermaux et al. 2022). The phenomenology of drop impact is extremely rich, encompassing behaviors such as drop

† Email address for correspondence: vatsalsanjay@gmail.com

‡ Email address for correspondence: binzhang0710@mail.tsinghua.edu.cn

¶ Email address for correspondence: cunjinglv@mail.tsinghua.edu.cn

|| Email address for correspondence: d.lohse@utwente.nl

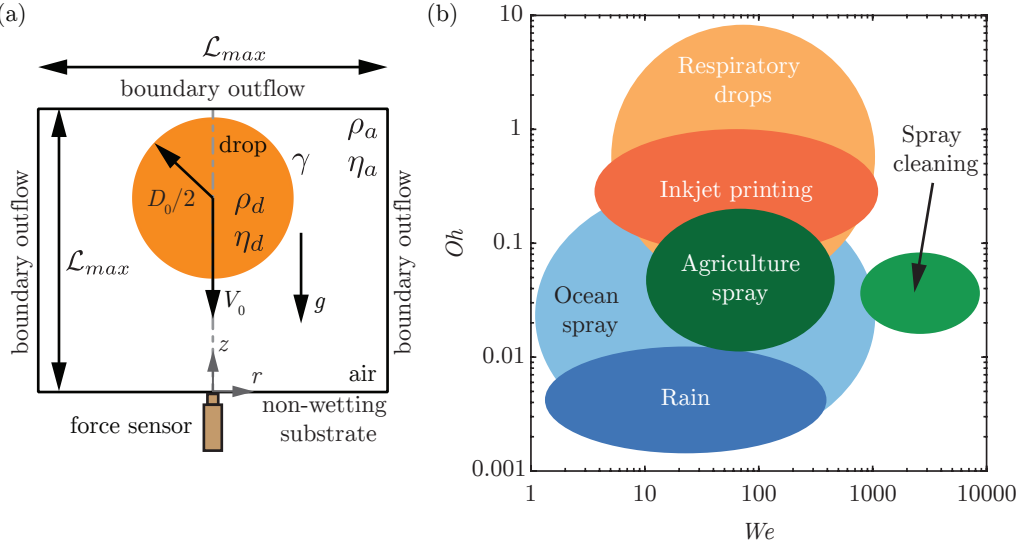


FIGURE 1. (a) Problem schematic with an axisymmetric computational domain used to study the impact of a drop with diameter D_0 and velocity V_0 on a non-wetting substrate. In the experiments, we use a quartz force sensor to measure the temporal variation of the impact force. The subscripts d and a denote the drop and air, respectively, to distinguish their material properties, which are the density ρ and the dynamic viscosity η . The drop-air surface tension coefficient is γ . The grey dashed-dotted line represents the axis of symmetry, $r = 0$. Boundary air outflow is applied at the top and side boundaries (tangential stresses, normal velocity gradient, and ambient pressure are set to zero). The domain boundaries are far enough from the drop not to influence its impact process ($L_{\max} \gg D_0$, $L_{\max} = 8R$ in the worst case). (b) The phase space with control parameters: the Weber number (We : dimensionless impact velocity) and the Ohnesorge number (Oh : dimensionless viscosity), exemplifying different applications.

deformation (Biance *et al.* 2006; Moláček & Bush 2012; Chevy *et al.* 2012), spreading (Laan *et al.* 2014; Wildeman *et al.* 2016), splashing Xu *et al.* (2005); Riboux & Gordillo (2014); Thoraval *et al.* (2021), fragmentation (Villermaux & Bossa 2011; Villermaux 2020), bouncing (Richard & Quéré 2000; Kolinski *et al.* 2014; Jha *et al.* 2020; Chubytsky *et al.* 2020; Sharma & Dixit 2021; Sanjay *et al.* 2023a), and wetting (de Gennes 1985; Fukai *et al.* 1995; Quéré 2008; Bonn *et al.* 2009). These behaviors are influenced by the interplay of inertial, capillary, and viscous forces, as well as additional factors like non-Newtonian properties (Bartolo *et al.* 2005, 2007; Smith & Bertola 2010; Gorin *et al.* 2022) of the liquid and even ambient air pressure (Xu *et al.* 2005), making the parameter space for this phenomenon both extensive and high-dimensional.

Naturally, even the process of a Newtonian liquid drop impacting a rigid substrate is governed by a plethora of control parameters, including but not limited to the drop's density ρ_d , diameter D_0 , velocity V_0 , dynamic viscosity η_d , surface tension γ , and acceleration due to gravity g (figure 1a). To navigate this rich landscape, we focus on two main dimensionless numbers that serve as control parameters (figure 1b): the Weber number We , which is the ratio of inertial to capillary forces and is given by

$$We = \frac{\rho_d V_0^2 D_0}{\gamma}, \quad (1.1)$$

and the Ohnesorge number Oh , which captures the interplay between viscous damping

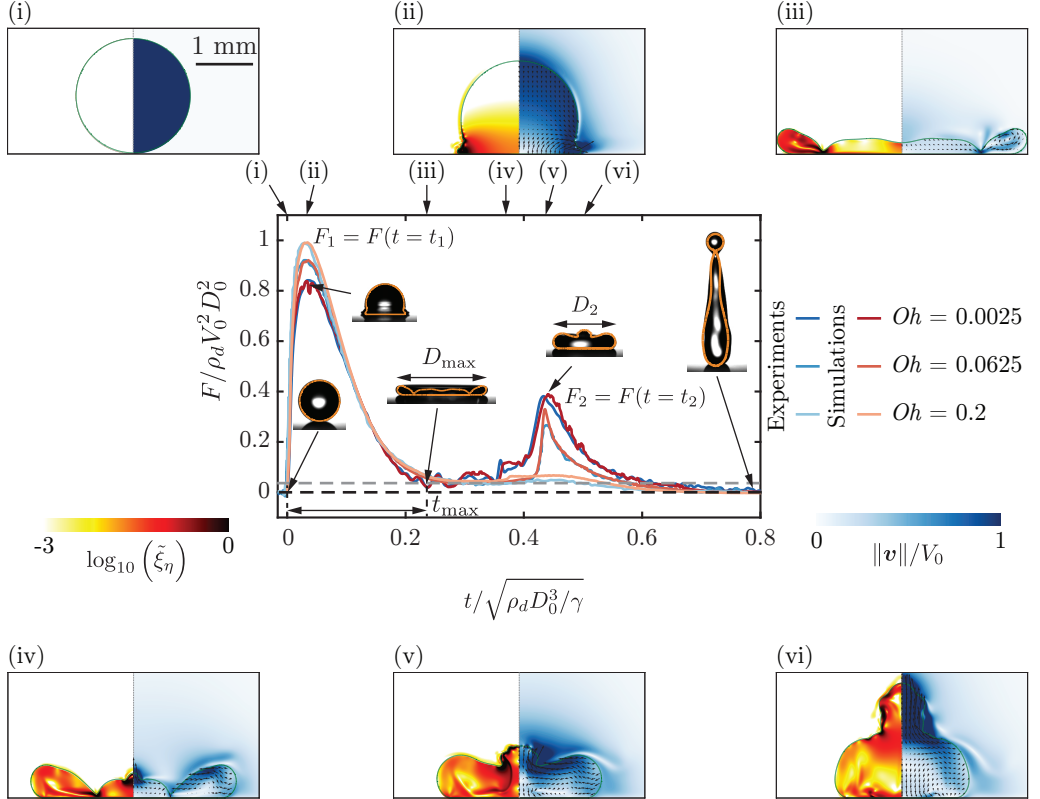


FIGURE 2. Comparison of the drop impact force $F(t)$ obtained from experiments and simulations for the three typical cases with impact velocity $V_0 = 1.2 \text{ m/s}$, 0.97 m/s , 0.96 m/s , diameter $D_0 = 2.05 \text{ mm}$, 2.52 mm , 2.54 mm , surface tension $\gamma = 72 \text{ mN/m}$, 61 mN/m , 61 mN/m and viscosity $\eta_d = 1 \text{ mPa s}$, 25.3 mPa s , 80.2 mPa s . These parameter give $Oh = 0.0025$, 0.0625 , 0.2 and $We = 40$. For the three cases, the two peak amplitudes, $F_1/\rho_d V_0^2 D_0^2 \approx 0.82$, 0.92 , 0.99 at $t_1 \approx 0.03\sqrt{\rho_d D_0^3/\gamma}$ and $F_2/\rho_d V_0^2 D_0^2 \approx 0.37$, 0.337 , 0.1 at $t_2 \approx 0.42\sqrt{\rho_d D_0^3/\gamma}$, characterize the inertial shock from impact and the Worthington jet before takeoff, respectively. The drop reaches the maximum spreading at t_{\max} when it momentarily stops and retracts until $t_3 \approx 0.8\sqrt{\rho_d D_0^3/\gamma}$ when the drop takes off ($F = 0$). Six instances are further elaborated through numerical simulations for ($We = 40$, $Oh = 0.0025$), namely (i) $t = 0 \text{ ms}$ (touch-down), (ii) $t = 0.37 \text{ ms}$ (t_1), (iii) $t = 2.5 \text{ ms}$ (t_{\max}), (iv) $t = 3.93 \text{ ms}$ ($\approx 0.85t_2$), (v) $t = 4.63 \text{ ms}$ (t_2), and (vi) $t = 5.25 \text{ ms}$ ($\approx 1.15t_2$). We stress the excellent agreement between experiments and simulations without any free parameters. The insets show representative snapshots at specific time instants overlaid with the drop boundaries from simulations in orange, also revealing good agreement. The left part of each numerical snapshot shows the dimensionless local viscous dissipation function $\tilde{\xi}_\eta \equiv \xi_\eta D_0 / (\rho_d V_0^3) = 2Oh(\tilde{\mathcal{D}} : \tilde{\mathcal{D}})$, where, \mathcal{D} is the symmetric part of the velocity gradient tensor, on a \log_{10} scale and the right part the velocity field magnitude normalized with the impact velocity. The black velocity vectors are plotted in the center of mass reference frame of the drop to clearly elucidate the internal flow.

and capillary oscillations, offering insights into how viscosity affects the drop's behavior upon impact,

$$Oh = \frac{\eta_d}{\sqrt{\rho_d \gamma D_0}}. \quad (1.2)$$

Additionally, the Bond number

$$Bo = \frac{\rho_d g D_0^2}{\gamma} \quad (1.3)$$

57 compares gravity to inertial forces and is needed to uniquely define the non-dimensional
58 problem.

59 The drop impact is not only interesting from the point of view of fundamental research
60 but also finds relevance in inkjet printing (Lohse 2022), the spread of respiratory drops
61 carrying airborne microbes (Bourouiba 2021; Ji *et al.* 2021; Pöhlker *et al.* 2023), cooling
62 applications (Kim 2007; Shiri & Bird 2017; Jowkar & Morad 2019), agriculture (Bergeron
63 *et al.* 2000; Bartolo *et al.* 2007; Kooij *et al.* 2018; Sijs & Bonn 2020; He *et al.* 2021;
64 Hoffman *et al.* 2021), criminal forensics (Smith *et al.* 2018; Smith & Brutin 2018), and
65 many other industrial and natural processes (Rein 1993; Yarin 2006; Tuteja *et al.* 2007;
66 Cho *et al.* 2016; Josserand & Thoroddsen 2016; Yarin *et al.* 2017; Liu *et al.* 2017; Hao
67 *et al.* 2016; Yarin *et al.* 2017; Wu *et al.* 2020). For these applications, it is pertinent to
68 understand the forces involved in drop impacts, as these forces can lead to soil erosion
69 (Nearing *et al.* 1986) or damage to engineered surfaces (Ahmad *et al.* 2013; Amirzadeh
70 *et al.* 2017; Gohardani 2011). We refer the readers to Cheng *et al.* (2022) for an overview
71 of the recent studies unraveling drop impact forces; see also Li *et al.* (2014); Soto *et al.*
72 (2014); Philippi *et al.* (2016); Zhang *et al.* (2017); Gordillo *et al.* (2018); Mitchell *et al.*
73 (2019); Zhang *et al.* (2019).

74 These forces have been studied by Zhang *et al.* (2022), employing experiments and
75 simulations and deriving scaling laws. A liquid drop impacting a non-wetting substrate
76 (figure 2i-vi) undergoes a series of phases—spreading, recoiling, and potentially rebounding
77 (Chantelot 2018)—driven by the normal reaction force exerted by the substrate. The
78 moment of touch-down (figure 2i-ii) (Wagner 1932; Philippi *et al.* 2016; Gordillo *et al.*
79 2018) is not surprisingly associated with a pronounced peak in the temporal evolution of
80 the drop impact force $F(t)$ owing to the sudden deacceleration as high as 100 times the
81 acceleration due to gravity (Clanet *et al.* 2004) (figure 2, $F(t = 0.37 \text{ ms}) \approx 5.1 \text{ mN}$). The
82 force diminishes as the drop reaches its maximum spreading diameter (figure 2iii). Zhang
83 *et al.* (2022) revealed that also the jump-off is accompanied by a peak in the normal
84 reaction force, which was up to then unknown (figure 2, $F_2(t_2 = 4.63 \text{ ms}) \approx 2.3 \text{ mN}$
85 for the second force peak amplitude—at time t_2 after impact). The second peak in the
86 force also coincides with the formation of a Worthington jet, a narrow upward jet of
87 liquid that can form due to flow focusing by the retracting drop (figure 2iv-vi). Under
88 certain conditions ($We \approx 9$), this peak can be even more pronounced than the first. This
89 discovery is critical for superhydrophobicity which is volatile and can fail due to external
90 disturbances such as pressure (Lafuma & Quéré 2003; Callies & Quéré 2005; Sbragaglia
91 *et al.* 2007; Li *et al.* 2017), evaporation (Tsai *et al.* 2010; Chen *et al.* 2012; Papadopoulos
92 *et al.* 2013), mechanical vibration (Bormashenko *et al.* 2007), or the impact forces of
93 prior droplets (Bartolo *et al.* 2006a).

94 In contrast to our prior study Zhang *et al.* (2022), which fixed the Ohnesorge number
95 to that of a 2 mm diameter water drop ($Oh = 0.0025$), our present investigation reported
96 in this paper explores a broader parameter space. We systematically and independently
97 vary the Weber and Ohnesorge numbers, extending the range of Oh to as high as 100.
98 This comprehensive approach enables us to develop new scaling laws and provides a
99 more unified understanding of the forces involved in drop impact problems. Our findings
100 are particularly relevant for applications with varying viscosities and impact velocities
101 (figure 1).

102 The structure of this paper is as follows: §2 briefly describes the experimental and

glycerol (wt %)	ρ_d (kg/m ³)	η_d (mPa.s)	γ (mN/m)
0	1000	1	72
50	1124	5	61
63	1158	10	61
74	1188	25.3	61
80	1200	45.4	61
85	1220	80.2	61

TABLE 1. Properties of the water-glycerol mixtures used in the experiments. ρ_d and η_d are the density and viscosity of the drop, respectively and γ denotes the liquid-air surface tension coefficient. These properties are calculated using the protocol provided in [Cheng \(2008\)](#); [Volk & Kähler \(2018\)](#).

numerical methods. §3 and §4 offer detailed analyses of the first and second peaks, respectively, focusing on their relationships with the Weber number (We) and the Ohnesorge number (Oh). Conclusions and perspectives for future research are presented in Section 5.

2. Methods

2.1. Experimental method

In the experimental setup, shown schematically in figure 1(a), a liquid drop impacts a superhydrophobic substrate. For water drops, such a surface is coated with silanized silica nanobeads with a diameter of 20 nm (Glaco Mirror Coat Zero; Soft99) resulting in the advancing and receding contact angles of $167 \pm 2^\circ$ and $154 \pm 2^\circ$, respectively ([Gauthier et al. 2015](#); [Li et al. 2017](#)). On the other hand, for viscous aqueous glycerin drops, the upper surface is coated with an acetone solution of hydrophobic beads (Ultra ever Dry, Ultratech International, a typical bead size of 20 nm), resulting in the advancing and receding contact angles of $166 \pm 4^\circ$ and $159 \pm 2^\circ$, respectively ([Jha et al. 2020](#)). The properties of the impacting drop are controlled using water-glycerol mixtures with viscosities η_d varying by almost two orders of magnitude, from 1 mPas to 80.2 mPas, yet maintaining a fairly constant surface tension γ and density ρ_d around 61 mN/m and 1000 kg/m³, respectively ([Cheng 2008](#); [Volk & Kähler 2018](#); [Jha et al. 2020](#)). Using other liquids like silicone oil could allow for a wider viscosity variation if used with a superamphiphobic substrate ([Deng et al. 2012](#)). The drop diameter D_0 is controlled between 2.05 mm and 2.76 mm by pushing it through a calibrated needle. Throughout this work, we use drops with diameter 2.54 ± 0.02 mm unless otherwise stated. Consequently, changing the viscosity of the drop determines the Ohnesorge number (Oh , see (1.2)). The Weber number (We , see (1.1)) is set using the impact velocity V_0 varying between 0.38 m/s and 2.96 m/s by changing the release height of the drops above the substrate. Lastly, we keep the Bond number (Bo , see (1.3)) fixed at 1 throughout the manuscript. In our system, the relevance of gravity is characterized by the dimensionless Froude number $Fr = V_0^2/gD_0 = We/Bo$ comparing inertia with gravity. Throughout this manuscript, $Fr > 1$ and gravity's role is sub-dominant compared to inertia. All experiments are conducted at ambient pressure and temperature. The impact force is directly measured using a high-precision piezoelectric force transducer (Kistler 9215A) with a resolution of 0.5 mN. During these measurements, the high-frequency vibrations induced by the measurement system and the surrounding noise are spectrally removed using a low pass

filter with a cut-off frequency of 5 kHz, following the procedure in Li *et al.* (2014); Zhang *et al.* (2017); Gordillo *et al.* (2018); Mitchell *et al.* (2019). The experiment also employs a high-speed camera (Photron Fastcam Nova S12) synchronized at 10,000 fps with a shutter speed 1/20,000 s. Throughout the manuscript, the error bars account for repeated trials and are visible if they are larger than the marker size. We refer the readers to the supplementary material of Zhang *et al.* (2022) for further details of the experimental setup.

2.2. Numerical framework

In the direct numerical simulations (DNS) employed for this study, the continuity and the momentum equations take the form

$$\nabla \cdot \mathbf{v} = 0 \quad (2.1)$$

and

$$\frac{\partial \mathbf{v}}{\partial t} + \nabla \cdot (\mathbf{v} \mathbf{v}) = \frac{1}{\rho} (-\nabla p + \nabla \cdot (2\eta \mathcal{D}) + \mathbf{f}_\gamma) + \mathbf{g}, \quad (2.2)$$

respectively. Here, \mathbf{v} is the velocity field, t is time, p is pressure, and \mathbf{g} is acceleration due to gravity. We use the free software program *Basilisk C* that employs the well-balanced geometric volume of fluid (VoF) method (Popinet 2009, 2018). The VoF tracer Ψ delineates the interface between the drop (subscript d , $\psi = 1$) and air (subscript a , $\psi = 0$), introducing a singular force $\mathbf{f}_\gamma \approx \gamma \kappa \nabla \Psi$ (κ denotes interfacial curvature, see Brackbill *et al.* 1992) to respect the dynamic boundary condition at the interface. This VoF tracer sets the material properties such that density ρ and viscosity η are given by

$$\rho = \rho_a + (\rho_d - \rho_a) \Psi \quad (2.3)$$

and

$$\eta = \eta_a + (\eta_d - \eta_a) \Psi, \quad (2.4)$$

respectively. This VoF field is advected with the flow, following the equation

$$\frac{\partial \Psi}{\partial t} + \nabla \cdot (\mathbf{v} \Psi) = 0. \quad (2.5)$$

Lastly, we calculate the normal reaction force $\mathbf{F}(t)$ by integrating the pressure field p at the substrate,

$$\mathbf{F}(t) = \left(\int_{\mathcal{A}} (p - p_0) d\mathcal{A} \right) \hat{\mathbf{z}}, \quad (2.6)$$

where, p_0 , $d\mathcal{A}$, and $\hat{\mathbf{z}}$ are the ambient pressure, substrate area element, and the unit vector normal to the substrate, respectively.

We leverage the axial symmetry of the drop impact (figure 1a). This axial symmetry breaks at large We (≥ 100 for water drops and even larger Weber number for more viscous drops), owing to destabilization by the surrounding gas after splashing (Xu *et al.* 2005; Eggers *et al.* 2010; Driscoll & Nagel 2011; Riboux & Gordillo 2014; Josserand &

Thoroddsen 2016; Zhang *et al.* 2022). To solve the governing equations (2.1)–(2.5), the velocity field \mathbf{v} and time t are normalized by the inertio-capillary scales, $V_\gamma = \sqrt{\gamma/\rho_d D_0}$ and $\tau_\gamma = \sqrt{\rho_d D_0^3/\gamma}$, respectively. Furthermore, the pressure is normalized using the capillary pressure scale $p_\gamma = \gamma/D_0$. In such a conceptualization, Oh and We described in §1 uniquely determine the system. The Ohnesorge number based on air viscosity $Oh_a = (\eta_a/\eta_d) Oh$ and air-drop density ratio ρ_a/ρ_d are fixed at 10^{-5} and 10^{-3} , respectively to minimize the influence of the surrounding medium on the impact forces. The substrate is modeled as a no-slip and non-penetrable wall, whereas vanishing stress and pressure are applied at the remaining boundaries to mimic outflow conditions for the surrounding air. The domain boundaries are far enough from the drop not to influence its impact process ($\mathcal{L}_{\max} \gg D_0$, $\mathcal{L}_{\max} = 8R$ in the worst case). At $t = 0$, in our simulations, we release a spherical drop whose south pole is $0.05D_0$ away from the substrate and is falling with a velocity V_0 . It is important to note that the drops may not be perfectly spherical and may have residual oscillations as they are released from the needle and arrive at the substrate. These oscillations are expected to be more pronounced for cases with small Weber and Ohnesorge numbers. The exact shape of the drop just before impact can influence the impact dynamics (Thoraval *et al.* 2013; Yun 2017). However, we suspect that the influence of these shape variations is captured, at least in part, by the error bars in the experimental data, which are derived from repeated trials under the same nominal conditions. The simulations utilize adaptive mesh refinement to finely resolve the velocity, viscous dissipation, and the VoF tracer fields. A minimum grid size $\Delta = D_0/2048$ is used for this study.

To ensure a perfectly non-wetting surface, we impose a thin air layer (minimum thickness $\sim \Delta/2$) between the drop and the substrate. This air layer prevents direct contact between the liquid and solid (Kolinski *et al.* 2014; Sprittles 2024), effectively mimicking a perfectly non-wetting surface. The presence of this air layer is crucial for capturing the dynamics of drop impact on superhydrophobic surfaces, as it allows for the formation of an air cushion that can significantly affect the spreading and rebound behavior of the drop (Ramírez-Soto *et al.* 2020; Sanjay *et al.* 2023a). While this approach does not fully resolve the microscopic dynamics within the air layer itself, such as the high-velocity gradients and viscous dissipation inside the gas film once it thins below a critical size ($\sim 10\Delta$), it has been shown to accurately capture the macroscopic behavior of drop impact in the parameter range of interest (Ramírez-Soto *et al.* 2020; Sanjay *et al.* 2023b; Alventosa *et al.* 2023a; García-Geijo *et al.* 2024). We refer the readers to Sanjay (2022) for discussions about this “precursor”, air film method and to Popinet & collaborators (2013–2023); Sanjay (2023); Zhang *et al.* (2022) for details on the numerical framework.

3. Anatomy of the first impact force peak

This section elucidates the anatomy of the first impact force peak and its relationship with the Weber We and Ohnesorge Oh numbers, first for the inertial limit (§3.1, $Oh \ll 1$) and then for the viscous asymptote (§3.2, $Oh \gg 1$). The results of this section are summarized in figure 3 that shows an excellent agreement between experiments and simulations without any free parameters.

3.1. Low Ohnesorge number impacts

For low Oh and large We , inertial force and time scales dictate the drop impact dynamics (figures 3 and 4). As the drop falls on a substrate, the part of the drop

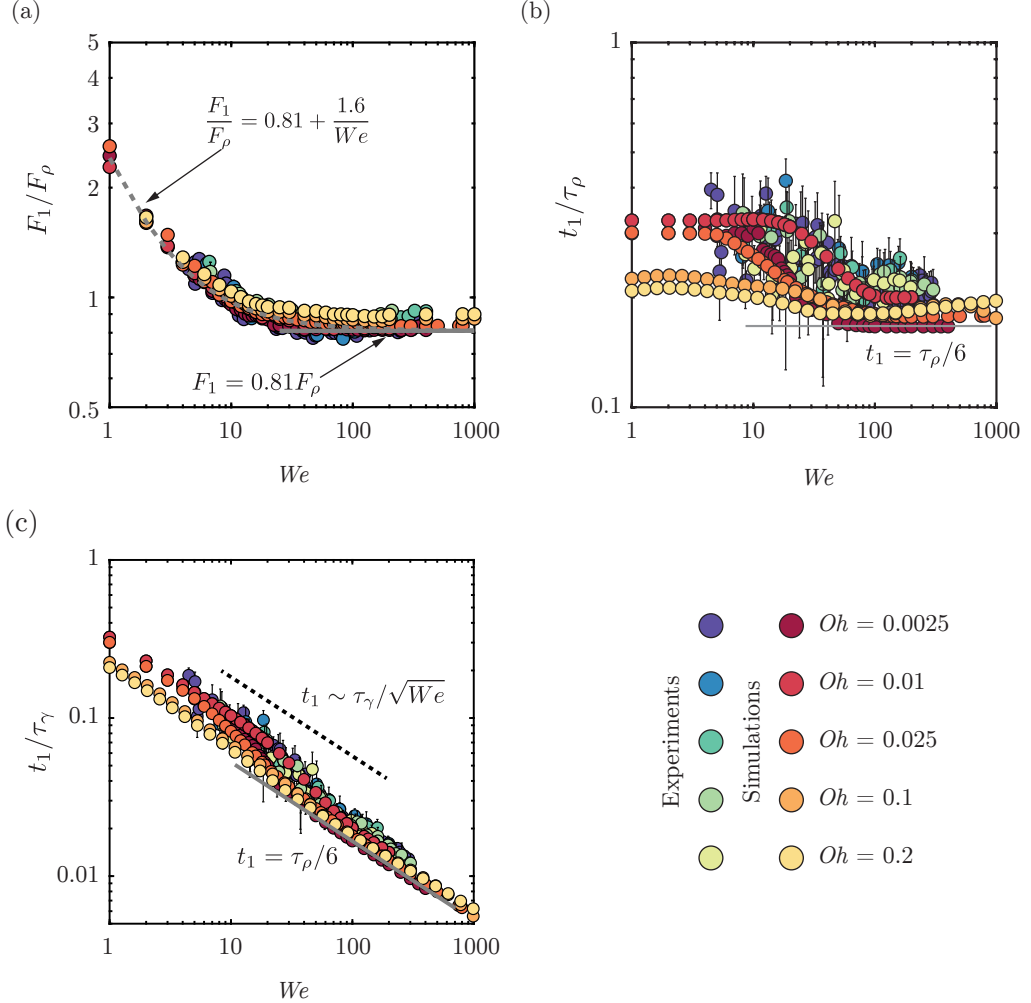


FIGURE 3. Anatomy of the first impact force peak amplitude at low Oh in between 0.0025 and 0.2, see color legend: We dependence of the (a) magnitude F_1 normalized by the inertial force scale $F_\rho = \rho_d V_0^2 D_0^2$ and time t_1 to reach the first force peak amplitude normalized by (b) the inertial timescale $\tau_\rho = D_0/V_0$ and (c) the inertia-capillary time scale $\tau_\gamma = \sqrt{\rho_d D_0^3/\gamma}$.

immediately in contact with the substrate stops moving, whereas the top of the drop still falls with the impact velocity (figure 4, from $t = t_1/4$ until $t = t_1$). Consequently, momentum conservation implies

$$F_1 \sim V_0 \frac{dm}{dt}, \quad (3.1)$$

where the mass flux $dm/dt \sim \rho_d V_0 D_0^2$ (Soto *et al.* 2014; Zhang *et al.* 2022). As a result, the first peak amplitude scales with the inertial pressure force (figure 3a)

$$F_1 \sim F_\rho, \text{ where } F_\rho = \rho_d V_0^2 D_0^2, \quad (3.2)$$

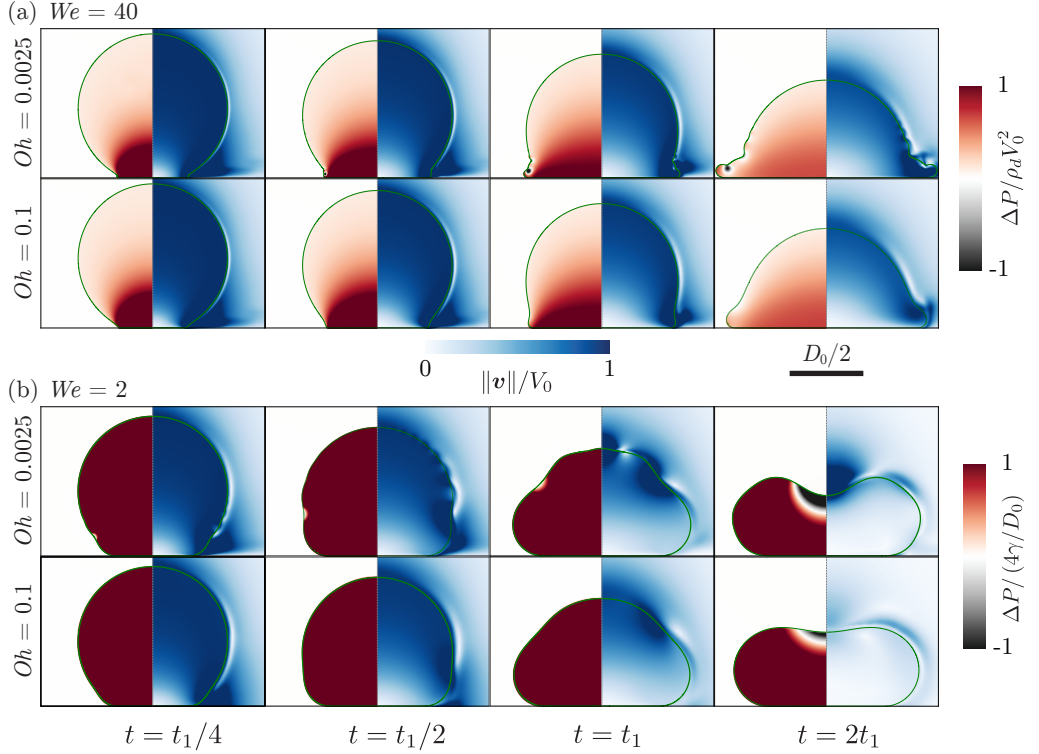


FIGURE 4. Direct numerical simulations snapshots illustrating the drop impact dynamics for $We =$ (a) 40 and (b) 2. The left-hand side of each numerical snapshot shows the pressure normalized by (a) the inertial pressure scale $\rho_d V_0^2$ and (b) the capillary pressure scale γ/D_0 . The right-hand side shows the velocity field magnitude normalized by the impact velocity V_0 .

for high Weber numbers ($We > 30$, $F_1 \approx 0.81F_\rho$). Furthermore, the time t_1 to reach F_1 follows

$$t_1 \sim \frac{D_0}{V_0} = \tau_\rho, \quad (3.3)$$

where, τ_ρ is the inertial timescale. The relation between equations (3.2) and (3.3) is apparent from the momentum conservation which implies that the impulse of the first force peak is equal to the momentum of the impacting drop, i.e., $F_1 t_1 \sim \rho_d V_0 D_0^3 = F_\rho \tau_\rho$ (see Gordillo *et al.* 2018, Zhang *et al.* 2022, and figures 3b,c). These scaling laws depend only on the inertial shock at impact and are wettability-independent (Zhang *et al.* 2017; Gordillo *et al.* 2018; Zhang *et al.* 2022). For details of the scaling law, including the prefactors, we refer the readers to Philippi *et al.* (2016); Gordillo *et al.* (2018); Cheng *et al.* (2022).

Figure 3 further illustrates that this inertial asymptote is insensitive to viscosity variations up to 100-fold as $F_1 \sim F_\rho$ and $t_1 \sim \tau_\rho$ for $0.0025 < Oh < 0.2$. However, deviations from the inertial force and time scales are apparent for $We < 30$ (figure 3), a phenomenon also reported in earlier work (Soto *et al.* 2014; Zhang *et al.* 2022). In these instances, inertia does not act as the sole governing force but instead complements surface tension, which dictates the pressure inside the drop ($p \sim \gamma/D_0$ throughout the drop for $We \lesssim 1$, figure 4b). Zhang *et al.* (2022) proposed an empirical functional dependence as

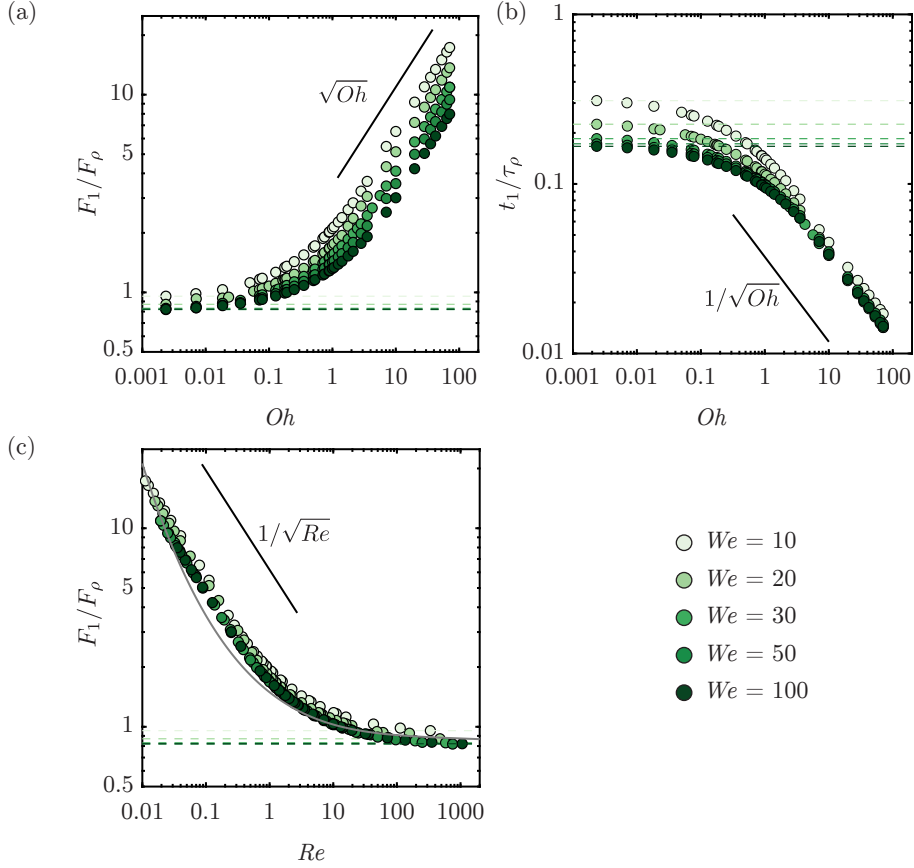


FIGURE 5. Anatomy of the first impact force peak amplitude for viscous impacts from our numerical simulations: the Oh dependence of (a) the magnitude F_1 normalized by the inertial force scale $\rho_d V_0^2 D_0^2$ and (b) the time t_1 to reach the first force peak amplitude normalized by inertial timescale $\tau_\rho = D_0/V_0$. (c) The Re dependence of the magnitude F_1 normalized by the inertial force scale $\rho_d V_0^2 D_0^2$ as compared to the (implicit) theoretical calculation of Gordillo *et al.* (2018). The black line corresponds to the scaling relationship described in §3.2. The Weber number is color-coded.

$$F_1 = \left(\alpha_1 \rho_d V_0^2 + \alpha_2 \frac{\gamma}{D_0} \right) D_0^2, \quad (3.4)$$

based on dimensional analysis, with α_1 and α_2 as free parameters which were determined to be approximately 1.6 and 0.81, respectively for water ($Oh = 0.0025$). These coefficients only deviate marginally in the current work despite the significant increase in Oh as compared to previous works (Cheng *et al.* 2022; Zhang *et al.* 2022). This consistency underscores the invariance of the pressure field inside the drop to an increase in Oh (close to the impact region, figure 4a and throughout the drop, figure 4b).

3.2. Large Ohnesorge number impacts

Figure 5 reaffirms the findings of §3.1 for low Oh that the first impact peak amplitude F_1 and the time to reach this peak amplitude t_1 scale with F_ρ and τ_ρ , respectively. As the Ohnesorge number increases further, the first impact force peak amplitude normalized

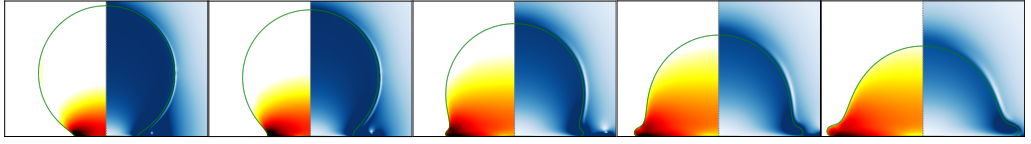
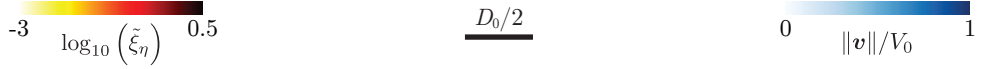
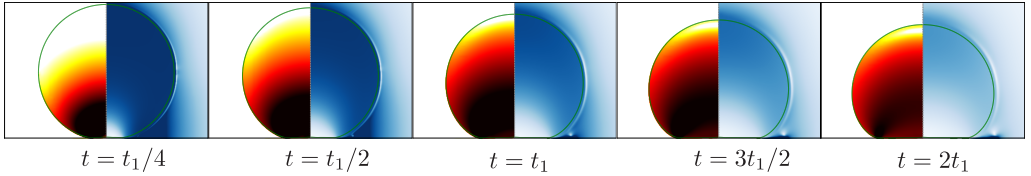
(a) $Oh = 0.05$ (b) $Oh = 0.5$ (c) $Oh = 5$ 

FIGURE 6. Direct numerical simulations snapshots illustrating the drop impact dynamics for $We = 100$ and $Oh =$ (a) 0.05, (b) 0.5, and (c) 5. The left-hand side of each numerical snapshot shows the viscous dissipation function ξ_η normalized by the inertial scale $\rho_d V_0^3 / D_0$. The right-hand side shows the velocity field magnitude normalized by the impact velocity V_0 .

with F_ρ begins to increase, indicating a transition around $Oh \approx 0.1$, where viscosity starts to play a significant role. At large Oh , we observe the scaling relationship (figure 5a)

$$F_1 \sim F_\rho \sqrt{Oh}. \quad (3.5)$$

The drop's momentum is still $\rho_d V_0 D_0^3$ which must be balanced by the impulse from the substrate, $F_1 t_1$ (see §3.1, Gordillo *et al.* 2018, Zhang *et al.* 2022, and figure 5b). Consequently, the time t_1 follows

$$t_1 \sim \frac{\tau_\rho}{\sqrt{Oh}}. \quad (3.6)$$

Figure 5 further shows that these scaling laws are weakly dependent on the Weber number, as viscous dissipation consumes the entire initial kinetic energy of the impacting drop (figure 6). Once again, we stress that using the water-glycerol mixtures limits the range of Oh that we can probe experimentally. We further note that the first peak is robust and does not depend on the wettability of the substrate. Consequently, to compare with the existing data such as those in Cheng *et al.* (2022) with different liquids to cover a wider range of liquid viscosities and to account for the apparent We -dependence, we plot F_1 compensated with F_ρ against the impact Reynolds number $Re \equiv \sqrt{We}/Oh = V_0 D_0 / \nu_d$. For the low Re regime, such a plot allows us to describe the We dependence on the prefactor more effectively, as illustrated in figure 5(c). However, it is important to note that some scatter is still observed at high Re values, which can be attributed to the We dependence of the impact force peak amplitude. This lack of a pure scaling behavior

259 demonstrates how the interplay between kinetic energy and viscous dissipation within
 260 the drop dictates the functional dependence of the maximum impact force on Oh .

261 To systematically elucidate these scaling behaviors in the limit of small Re , we need
 262 to find the typical scales for the rate of change of kinetic energy and that of the rate of
 263 viscous dissipation for the drop impact system. First, we can readily define an average
 264 rate of viscous dissipation per unit mass as

$$\bar{\varepsilon} \sim \frac{1}{\tau_\rho} \frac{1}{D_0^3} \int_0^{\tau_\rho} \int_{\Omega} \nu_d (\mathcal{D} : \mathcal{D}) d\Omega dt, \quad (3.7)$$

265 where ν_d is the kinematic viscosity of the drop and $d\Omega$ is the volume element where
 266 dissipation occurs. Notice that $\bar{\varepsilon}$ has the dimensions of V_0^3/D_0 , i.e., length squared over
 267 time cubed or velocity squared over time, as it should be for dissipation rate of energy
 268 per unit mass. We can estimate $\Omega = D_{\text{foot}}^2 l_\nu$ (figure 6), where D_{foot} is the drop's foot
 269 diameter in contact with the substrate and l_ν is the viscous boundary layer thickness.
 270 This boundary layer marks the region of strong velocity gradients ($\sim V_0/l_\nu$) analogous to
 271 the Mirels (1955) shockwave-induced boundary layer. For details, we refer the authors to
 272 Schlichting (1968); Schroll *et al.* (2010); Philippi *et al.* (2016). Consequently, the viscous
 273 dissipation rate scales as

$$\bar{\varepsilon} \sim \frac{1}{\tau_\rho D_0^3} \int_0^{\tau_\rho} \nu_d \left(\frac{V_0}{l_\nu} \right)^2 D_{\text{foot}}^2 l_\nu dt. \quad (3.8)$$

274 To calculate D_{foot} , we assume that the drop maintains a spherical cap shape throughout
 275 the impact (figure 6). To calculate the distance the drop would have traveled if there
 276 were no substrate, we use the relation $d \sim V_0 t$. Simple geometric arguments allow us
 277 to determine the relation between the foot diameter and this distance, $D_{\text{foot}} \sim \sqrt{D_0 d}$
 278 (Lesser 1981; Mandre *et al.* 2009; Zheng *et al.* 2021; Bilotto *et al.* 2023; Bertin 2023).
 279 Interestingly, this scaling behavior is similar to the inertial limit (Wagner 1932; Bouwhuis
 280 *et al.* 2012; Philippi *et al.* 2016; Gordillo *et al.* 2019) as discussed by Langley *et al.* (2017);
 281 Bilotto *et al.* (2023). Furthermore, the viscous boundary layer l_ν can be approximated
 282 using $\sqrt{\nu_d t}$ (Mirels 1955; Eggers *et al.* 2010; Philippi *et al.* 2016). Filling these in (3.8),
 283 we get

$$\bar{\varepsilon} \sim \frac{1}{\tau_\rho D_0^2} \int_0^{\tau_\rho} \sqrt{\nu_d} V_0^3 \sqrt{t} dt, \quad (3.9)$$

284 which on integration gives

$$\bar{\varepsilon} \sim \sqrt{\nu_d \tau_\rho} V_0^3 / D_0^2, \quad (3.10)$$

285 where τ_ρ is the inertial time scale. Here, we assume that for highly viscous drops, all
 286 energy is dissipated within a fraction of τ_ρ . Filling in (3.10) and normalizing $\bar{\varepsilon}$ with the
 287 inertial scales V_0^3/D_0 ,

$$\frac{\bar{\varepsilon}}{V_0^3/D_0} \sim \sqrt{\frac{\nu_d \tau_\rho}{D_0^2}} = \frac{1}{\sqrt{Re}} = \left(\frac{Oh}{\sqrt{We}} \right)^{1/2}. \quad (3.11)$$

288 Next, the kinetic energy of the falling drop is given by

$$\dot{K}(t) \equiv \frac{dK(t)}{dt} \sim \rho_d D_0^3 \bar{\varepsilon}, \quad \text{where } K(t) = \frac{1}{2} m (V(t))^2, \quad (3.12)$$

and $V(t)$ is the drop's center of mass velocity. The left-hand side of (3.12) can be written as

$$\dot{K}(t) = m V(t) \frac{dV(t)}{dt} = F(t) V(t). \quad (3.13)$$

In equation (3.13), $F(t)$ and $V(t)$ scale with the first impact force peak amplitude F_1 and the impact velocity V_0 , respectively, giving the typical scale of the rate of change of kinetic energy as

$$\dot{K}^* \sim F_1 V_0. \quad (3.14)$$

We stress that (3.14) states that the rate of change of kinetic energy is equal to the power of the normal reaction force, an observation already made by Wagner (1932) and Philippi *et al.* (2016) in the context of impact problems. Lastly, at large Oh , viscous dissipation enervates kinetic energy completely giving (figure 6c, also see: Philippi *et al.* (2016) and Wildeman *et al.* (2016)),

$$\dot{K}^* \sim F_1 V_0 \sim \rho_d D_0^3 \bar{\varepsilon} \quad (3.15)$$

Additionally, we use the inertial scales to non-dimensionalize (3.15) and fill in (3.11), giving

$$\frac{F}{F_\rho} \sim \frac{\bar{\varepsilon}}{V_0^3/D_0} \sim \frac{1}{\sqrt{Re}} = \left(\frac{Oh}{\sqrt{We}} \right)^{1/2} \quad (3.16)$$

and using $F_1 t_1 \sim \rho_d V_0 D_0^3 = F_\rho \tau_\rho$,

$$\frac{t_1}{\tau_\rho} \sim \left(\frac{\sqrt{We}}{Oh} \right)^{1/2}. \quad (3.17)$$

In summary, we use energy and momentum invariance to elucidate the parameter dependencies of the impact force as illustrated in figure 5. The scaling arguments capture the dominant force balance during the impact process, considering the relative importance of inertial, capillary, and viscous forces. As the dimensionless viscosity of impacting drops increases, the lack of surface deformation increases the normal reaction force (3.16). Further, the invariance of incoming drop momentum implies that this increase in normal reaction force occurs on a shorter timescale (3.17).

4. Anatomy of the second impact force peak

This section delves into the anatomy of the second impact force peak amplitude F_2 as a function of the Weber We and Ohnesorge Oh numbers, summarized in figure 7. We once again note the remarkable agreement between experiments and numerical simulations in this figure.

Similar to the mechanism leading to the formation of the first peak (§3), also the

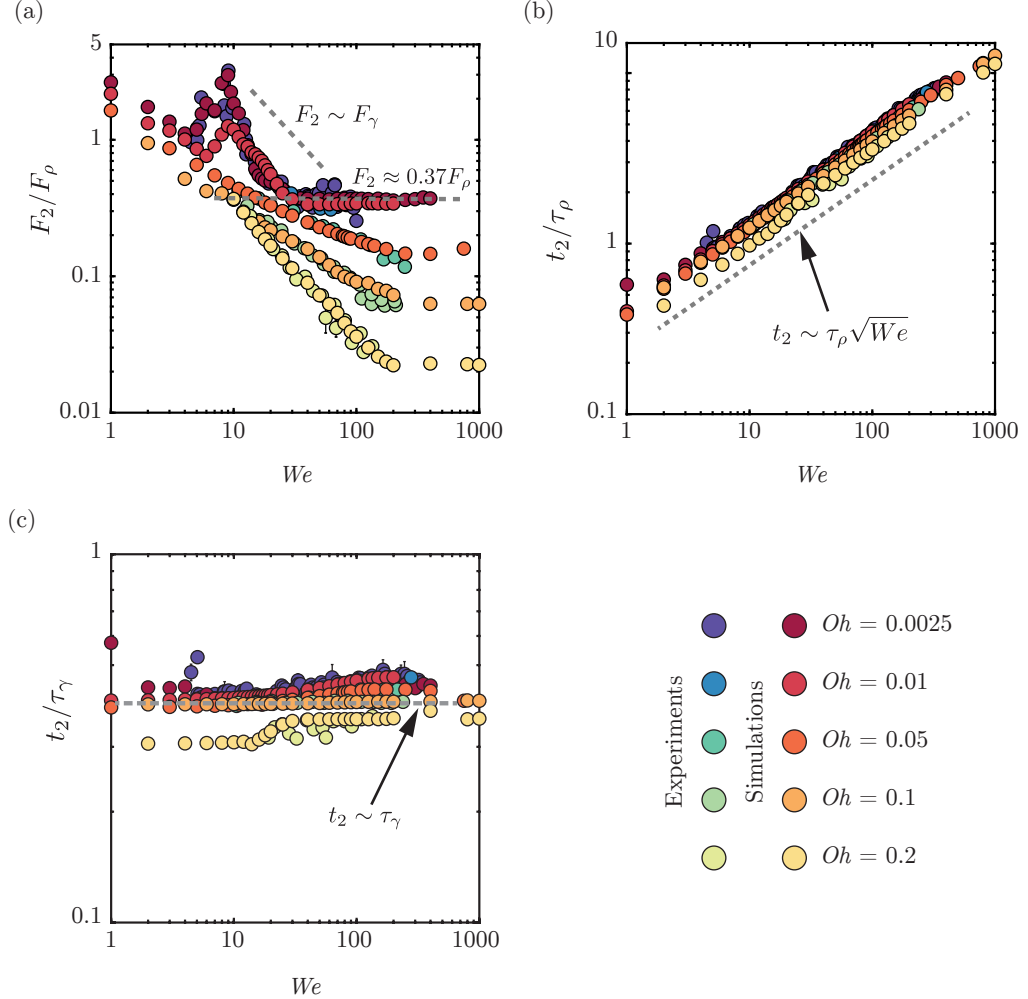


FIGURE 7. Anatomy of the second impact force peak amplitude: We dependence of the (a) magnitude F_2 normalized by the inertial force scale $F_\rho = \rho_d V_0^2 D_0^2$ and time t_2 to reach the second force peak amplitude normalized by (b) the inertio-capillary time scale $\tau_\gamma = \sqrt{\rho_d D_0^3 / \gamma}$ and (c) inertial timescale $\tau_\rho = D_0 / V_0$.

mechanism for the formation of this second peak is momentum conservation. As the drop takes off the surface, it applies a force on the substrate. As noted in §1 and Zhang *et al.* (2022), this force also coincides with the formation of a Worthington jet (figure 2iv). The time t_2 at which the second peak is observed scales with the inertio-capillary timescale and is insensitive to We and Oh (figure 7b,c). Once again, we invoke the analogy between drop oscillation and drop impact to explain this behavior (Richard *et al.* 2002; Chevy *et al.* 2012). At the time instant $t_2 \approx 0.44\tau_\gamma$, the drop's internal motion undergoes a transition from a predominantly radial flow to a vertical one due to the formation of the Worthington jet (Chantelot 2018; Zhang *et al.* 2022). Figure 8 exemplifies this jet in the $Oh - We$ parameter space, which is intricately related to the second peak in the drop impact force. For low Oh and large We , the drop retraction follows a modified Taylor-Culick dynamics (Bartolo *et al.* 2005; Eggers *et al.* 2010; Sanjay *et al.* 2022). As We is

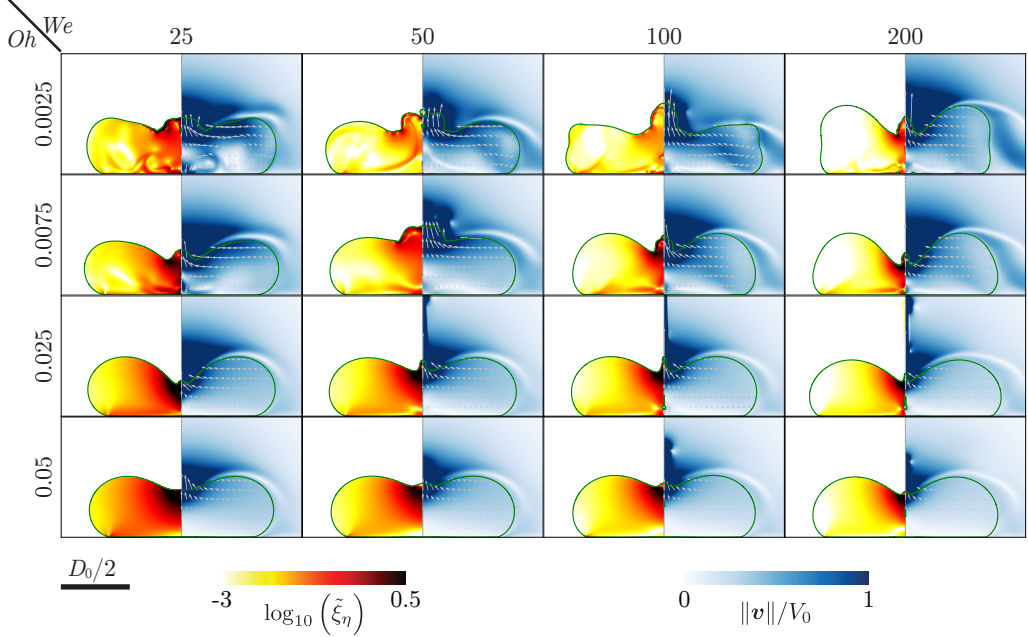


FIGURE 8. Direct numerical simulations snapshots illustrating the influence of We and Oh on the inception of the Worthington jet. All these snapshots are taken at the instant when the second peak appears in the temporal evolution of the normal reaction force ($t = t_2$). The left-hand side of each numerical snapshot shows the viscous dissipation function ξ_η normalized by the inertial scale $\rho_d V_0^3 / D_0$. The right-hand side shows the velocity field magnitude normalized by the impact velocity V_0 . The gray velocity vectors are plotted in the center of mass reference frame of the drop to clearly elucidate the internal flow.

increased, the jet gets thinner but faster, maintaining a constant momentum flux $\rho_d V_j^2 d_j^2$, where V_j and d_j are the jet's velocity and diameter, respectively (figure 8, Zhang *et al.* 2022). This invariance leads to the observed scaling $F_2 \sim F_\rho$ in this regime ($F_2 \approx 0.37 F_\rho$ for $We \geq 30, Oh \leq 0.01$).

Furthermore, the low We and Oh regime relies entirely on capillary pressure (figure 4). Subsequently, $F_2 \sim F_\gamma = \gamma D_0$ for $Oh < 0.01$ and $We < 30$ (figure 7). This flow focusing (figure 8) is most efficient for $We = 9$ (figure 9a, $t_2/2 < t < t_2$, Renardy *et al.* 2003; Bartolo *et al.* 2006b) where the capillary resonance leads to a thin-fast jet, accompanied by a bubble entrainment, reminiscent of the hydrodynamic singularity (figure 9, Zhang *et al.* 2022; Sanjay *et al.* 2021). The characteristic feature of this converging flow is a higher magnitude of F_2 compared to F_1 (figure 7).

However, this singular jet regime is very narrow in the $Oh - We$ phase space. Figure 9b shows two cases for water drops ($Oh = 0.0025$) at different We (5 and 12 for figures 9b-i and b-ii, respectively). Bubble entrainment does not occur in either of these cases. Consequently, the maximum force amplitude diminishes for these two cases (figure 7). Nonetheless, these cases are still associated with high local viscous dissipation near the axis of symmetry owing to the singular nature of the flow. Another mechanism to inhibit this singular Worthington jet is viscous dissipation in the bulk. As the Ohnesorge number increases, this singular jet formation disappears ($Oh = 0.005$, figure 9c-i), significantly reducing the second peak of the impact force. For even higher viscosities, the drop no longer exhibits the sharp, focused jet formation seen at lower viscosities, and the second peak in the force is notably diminished ($Oh = 0.05$, figure 9c-ii).

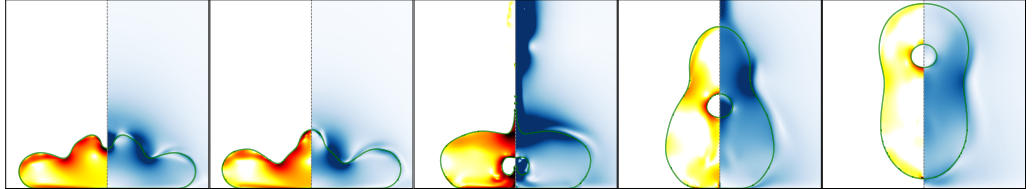
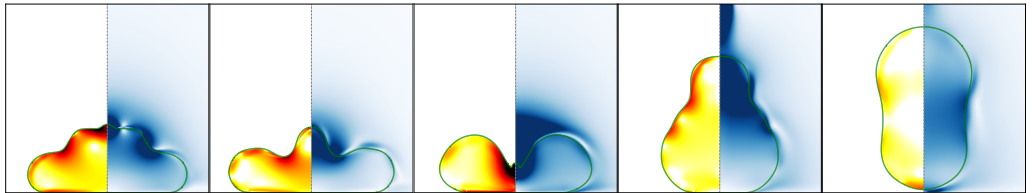
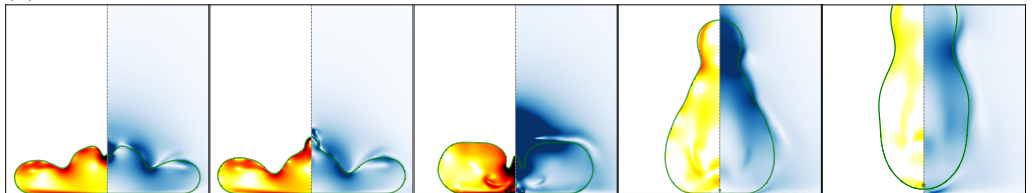
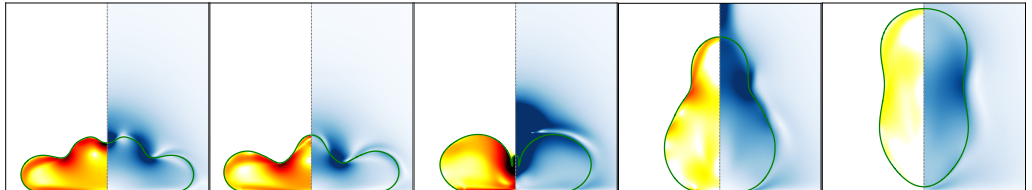
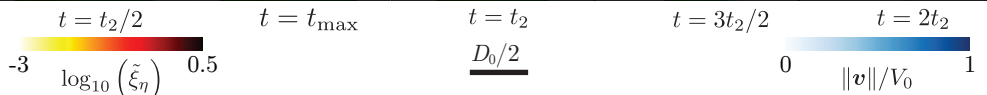
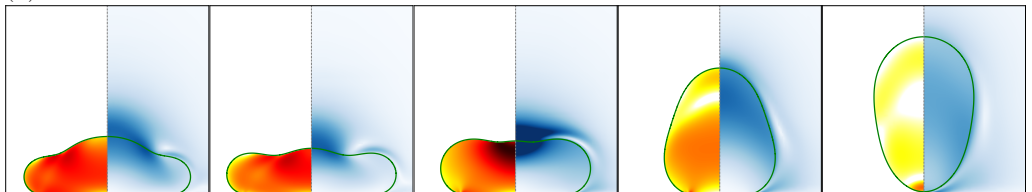
(a) $We = 9, Oh = 0.0025$ (b) $Oh = 0.0025$ (i) $We = 5$ (ii) $We = 12$ (c) $We = 9$ (i) $Oh = 0.005$ (ii) $Oh = 0.05$ 

FIGURE 9. Direct numerical simulations snapshots illustrating the influence of We and Oh on the singular Worthington jet. (a) $(We, Oh) = (9, 0.0025)$, (b) $Oh = 0.0025$ with $We =$ (i) 5 and (ii) 12, and (c) $We = 9$ with $Oh =$ (i) 0.005 and (ii) $Oh = 0.05$. The left-hand side of each numerical snapshot shows the viscous dissipation function ξ_η normalized by inertial scale $\rho_d V_0^3 / D_0$. The right-hand side shows the velocity field magnitude normalized by the impact velocity V_0 .

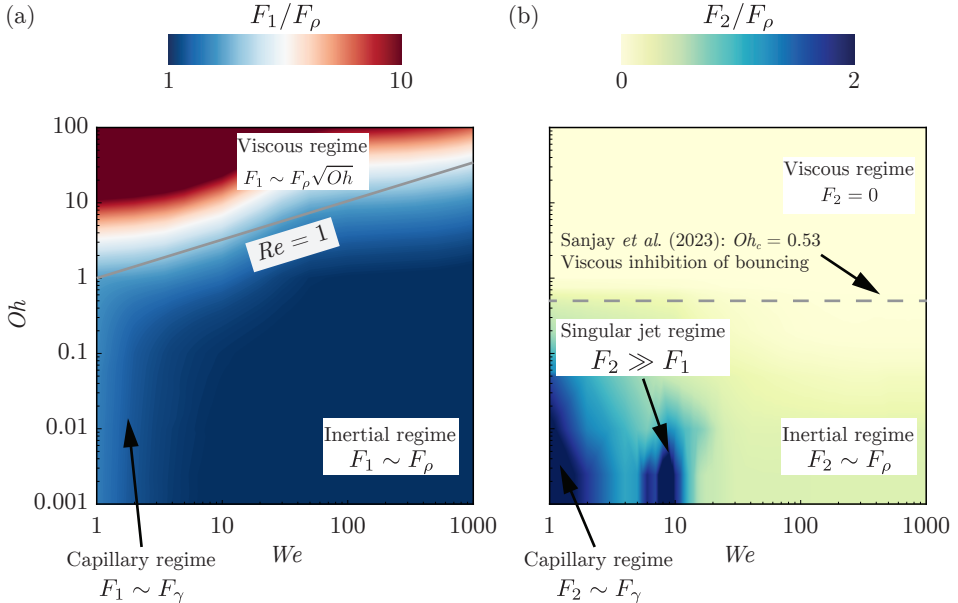


FIGURE 10. Regime map in terms of the drop Ohnesorge number Oh and the impact Weber number We to summarize the two peaks in the impact force by showing the different regimes described in this work based on (a) the first peak in the impact force peak amplitude F_1 and (b) the second peak in the impact force peak amplitude F_2 . Both peaks are normalized by the inertial force scale $F_\rho = \rho_d V_0^2 D_0^2$. These regime maps are constructed using ~ 1500 simulations in the range $0.001 \leq Oh \leq 100$ and $1 \leq We \leq 1000$. The gray solid line in (a) and dashed line in (b) mark the inertial-viscous transition ($Re = 1$) and the bouncing-no-bouncing transition ($Oh_c = 0.53$ for $Bo = 1$, see [Sanjay et al. \(2023a\)](#)), respectively.

Lastly, as Oh increases, bulk dissipation becomes dominant (apparent from increasing Oh at fixed We in figure 8) and can entirely inhibit drop bouncing. Recently, [Jha et al. \(2020\)](#); [Sanjay et al. \(2023a\)](#) showed that there exists a critical Oh , two orders of magnitude higher than that of a 2 mm diameter water drop, beyond which drops do not bounce either, irrespective of their impact velocity. Consequently, the second peak in the impact force diminishes for larger Oh , which explains the monotonic decrease of the amplitude F_2 observed in figure 7 for $We > 30, Oh > 0.01$.

5. Conclusion and outlook

In this work, we study the forces and dissipation encountered during the drop impact process by employing experiments, numerical simulations, and theoretical scaling laws. We vary the two dimensionless control parameters—the Weber (We : dimensionless impact velocity) and the Ohnesorge number (Oh : dimensionless viscosity) independently to elucidate the intricate interplay between inertia, viscosity, and surface tension in governing the forces exerted by a liquid drop upon impact on a non-wetting substrate.

For the first impact force peak amplitude F_1 , owing to the momentum balance after the inertial shock at impact, figure 10(a) summarizes the different regimes in the $Oh - We$ phase space. For low Oh , inertial forces predominantly dictate the impact dynamics, such that F_1 scales with the inertial force F_ρ ([Philippi et al. 2016](#); [Gordillo et al. 2018](#); [Mitchell et al. 2019](#); [Cheng et al. 2022](#); [Zhang et al. 2022](#)) and is insensitive to viscosity variations up to 100-fold. As Oh increases, the viscosity becomes significant, leading to a new scaling law: $F_1 \sim F_\rho \sqrt{Oh}$. The paper unravels this viscous scaling behavior by accounting for

370 the loss of initial kinetic energy owing to viscous dissipation inside the drop. Lastly, at
 371 low We , the capillary pressure inside the drop leads to the scaling $F_1 \sim F_\gamma$ (Moláček &
 372 Bush 2012; Chevy *et al.* 2012).

373 The normal reaction force described in this work is responsible for deforming the
 374 drop as it spreads onto the substrate, where it stops thanks to surface tension. If the
 375 substrate is non-wetting, it retracts to minimize the surface energy and finally takes off
 376 (Richard & Quéré 2000). In this case, the momentum conservation leads to the formation
 377 of a Worthington jet and a second peak in the normal reaction force, as summarized in
 378 figure 10(b). For low Oh and high We , the second force peak amplitude scales with the
 379 inertial force (F_ρ), following a modified Taylor-Culick dynamics (Eggers *et al.* 2010). In
 380 contrast, capillary forces dominate at low We and low Oh , leading to a force amplitude
 381 scaling of $F_2 \sim F_\gamma$. We also identify a narrow regime in the $Oh - We$ phase space
 382 where a singular Worthington jet forms, significantly increasing F_2 (Bartolo *et al.* 2006b;
 383 Zhang *et al.* 2022), localized in the parameter space for $We \approx 9$ and $Oh < 0.01$. As Oh
 384 increases, bulk viscous dissipation counteracts this jet formation, diminishing the second
 385 peak and ultimately inhibiting drop bouncing.

386 Our findings have far-reaching implications, not only enriching the fundamental
 387 understanding of fluid dynamics of drop impact but also informing practical applications
 388 in diverse fields such as inkjet printing, public health, agriculture, and material science
 389 where the entire range of $Oh - We$ phase space is relevant (figures 1b and 10). While this
 390 has identified new scaling laws, it also opens avenues for future research. For instance,
 391 it would be interesting to use the energy accounting approach to unify the scaling laws
 392 for the maximum spreading diameter for arbitrary Oh (Laan *et al.* 2014; Wildeman
 393 *et al.* 2016). Although, the implicit theoretical model summarized in Cheng *et al.* (2022)
 394 describes most of data in figure 5, we stress the importance of having a predictive model
 395 to determine F_1 for given We and Oh (Sanjay & Lohse 2024). The We influence on
 396 the impact force also warrants further exploration, especially in the regime $We \ll 1$ for
 397 arbitrary Oh (Chevy *et al.* 2012; Moláček & Bush 2012) and drop impact on compliant
 398 surfaces (Alventosa *et al.* 2023b; Ma & Huang 2023). Another potential extension of this
 399 work is to non-Newtonian fluids (Martouzet *et al.* 2021; Agüero *et al.* 2022; Bertin 2023;
 400 Jin *et al.* 2023).

401
 402 **Code availability.** The codes used in the present article are permanently available at
 403 Sanjay (2023).

404
 405 **Acknowledgements.** We would like to thank Vincent Bertin for comments on the
 406 manuscript. We would also like to thank Andrea Prosperetti, Pierre Chantelot, Devaraj
 407 van der Meer, and Uddalok Sen for illuminating discussions.

408
 409 **Funding.** We acknowledge the funding by the ERC Advanced Grant No. 740479-DDD
 410 and NWO-Canon grant FIP-II. B.Z and C.L are grateful for the support from National
 411 Natural Science Foundation of China (Grant No. 12172189, 11921002, 11902179). This
 412 work was carried out on the national e-infrastructure of SURFsara, a subsidiary of SURF
 413 cooperation, the collaborative ICT organization for Dutch education and research. This
 414 work was sponsored by NWO - Domain Science for the use of supercomputer facilities.

415
 416 **Declaration of Interests.** The authors report no conflict of interest.

Author ORCID.

- V. Sanjay <https://orcid.org/0000-0002-4293-6099>;
 B. Zhang <https://orcid.org/0000-0001-8550-2584>;
 C. Lv <https://orcid.org/0000-0001-8016-6462>;
 D. Lohse <https://orcid.org/0000-0003-4138-2255>.

REFERENCES

- AGÜERO, E. A., ALVENTOSA, L. F. L., HARRIS, D. M. & GALEANO-RIOS, C. A. 2022 Impact of a rigid sphere onto an elastic membrane. *Proc. R. Soc. Lond. A* **478** (2266), 20220340.
- AHMAD, M., SCHATZ, M. & CASEY, M. V. 2013 Experimental investigation of droplet size influence on low pressure steam turbine blade erosion. *Wear* **303**, 83–86.
- ALVENTOSA, L. F. L., CIMPEANU, R. & HARRIS, D. M. 2023a Inertio-capillary rebound of a droplet impacting a fluid bath. *J. Fluid Mech.* **958**, A24.
- ALVENTOSA, L. F. L., CIMPEANU, R. & HARRIS, D. M. 2023b Inertio-capillary rebound of a droplet impacting a fluid bath. *J. Fluid Mech.* **958**, A24.
- AMIRZADEH, B., LOUGHALAM, A., RAESSI, M. & TOOTKABONI, M. 2017 A computational framework for the analysis of rain-induced erosion in wind turbine blades. *J. Wind Eng. Ind. Aerodyn.* **163**, 33–43.
- BARTOLO, D., BOUAMRIRENE, F., VERNEUIL, E., BUGUIN, A., SILBERZAN, P. & MOULINET, S. 2006a Bouncing or sticky droplets: Impalement transitions on superhydrophobic micropatterned surfaces. *Europhys. Lett.* **74** (2), 299.
- BARTOLO, D., BOUDAOU, A., NARCY, G. & BONN, D. 2007 Dynamics of non-Newtonian droplets. *Phys. Rev. Lett.* **99** (17), 174502.
- BARTOLO, D., JOSSERAND, C. & BONN, D. 2005 Retraction dynamics of aqueous drops upon impact on non-wetting surfaces. *J. Fluid Mech.* **545**, 329–338.
- BARTOLO, D., JOSSERAND, C. & BONN, D. 2006b Singular jets and bubbles in drop impact. *Phys. Rev. Lett.* **96** (12), 124501.
- BERGERON, V., BONN, D., MARTIN, J. Y. & VOVELLE, L. 2000 Controlling droplet deposition with polymer additives. *Nature* **405** (6788), 772–775.
- BERNY, A., POPINET, S., SÉON, T. & DEIKE, L. 2021 Statistics of jet drop production. *Geophys. Res. Lett.* **48** (10), e2021GL092919.
- BERTIN, V. 2023 Similarity solutions in elastohydrodynamic bouncing. *arXiv preprint arXiv:2308.10754*.
- BIANCE, A.-L., CHEVY, F., CLANET, C., LAGUBEAU, G. & QUÉRÉ, D. 2006 On the elasticity of an inertial liquid shock. *J. Fluid Mech.* **554**, 47–66.
- BILOTTO, J., KOLINSKI, J. M., LECAMPION, B., MOLINARI, J.-F., SUBHASH, G. & GARCIA-SUAREZ, J. 2023 Fluid-mediated impact of soft solids. *arXiv preprint arXiv:2311.09953*.
- BONN, D., EGGERS, J., INDEKEU, J., MEUNIER, J. & ROLLEY, E. 2009 Wetting and spreading. *Rev. Mod. Phys.* **81** (2), 739–805.
- BORMASHENKO, E., POGREB, R., WHYMAN, G. & ERLICH, M. 2007 Resonance Cassie-Wenzel wetting transition for horizontally vibrated drops deposited on a rough surface. *Langmuir* **23** (24), 12217–12221.
- BOUROUIBA, L. 2021 The fluid dynamics of disease transmission. *Annu. Rev. Fluid Mech.* **53**, 473–508.
- BOUWHUIS, W., VAN DER VEEN, R. C. A., TRAN, T., KEIJ, D. L., WINKELS, K. G., PETERS, I. R., VAN DER MEER, D., SUN, C., SNOEIJER, J. H. & LOHSE, D. 2012 Maximal air bubble entrainment at liquid-drop impact. *Phys. Rev. Lett.* **109** (26), 264501.
- BRACKBILL, J. U., KOTHE, D. B. & ZEMACH, C. 1992 A continuum method for modeling surface tension. *J. Comput. Phys.* **100** (2), 335–354.
- CALLIES, M. & QUÉRÉ, D. 2005 On water repellency. *Soft Matter* **1** (1), 55–61.
- CHANTELLOT, P. 2018 Rebonds spéciaux de liquides. PhD thesis, Université Paris-Saclay (ComUE).
- CHEN, X., MA, R., LI, J., HAO, C., GUO, W., LUK, B. L., LI, S. C., YAO, S. & WANG, Z.

- 471 2012 Evaporation of droplets on superhydrophobic surfaces: surface roughness and small
472 droplet size effects. *Phys. Rev. Lett.* **109** (11), 116101.
- 473 CHENG, N.-S. 2008 Formula for the viscosity of a glycerol–water mixture. *Ind. Eng. Chem. Res.*
474 **47** (9), 3285–3288.
- 475 CHENG, X., SUN, T.-P. & GORDILLO, L. 2022 Drop impact dynamics: impact force and stress
476 distributions. *Annu. Rev. Fluid Mech.* **54**, 57–81.
- 477 CHEVY, F., CHEPELIANSKII, A., QUÉRÉ, D. & RAPHAËL, E. 2012 Liquid Hertz contact: softness
478 of weakly deformed drops on non-wetting substrates. *Europhys. Lett.* **100** (5), 54002.
- 479 CHO, H. J., PRESTON, D. J., ZHU, Y. & WANG, E. N. 2016 Nanoengineered materials for
480 liquid–vapour phase-change heat transfer. *Nat. Rev. Mater.* **2** (2), 16092.
- 481 CHUBYNSKY, M. V., BELOUSOV, K. I., LOCKERBY, D. A. & SPRITTLES, J. E. 2020 Bouncing
482 off the walls: the influence of gas-kinetic and van der Waals effects in drop impact. *Phys.*
483 *Rev. Lett.* **124**, 084501.
- 484 CLANET, C., BÉGUIN, C., RICHARD, D. & QUÉRÉ, D. 2004 Maximal deformation of an
485 impacting drop. *J. Fluid Mech.* **517**, 199–208.
- 486 DA VINCI, L. 1508 *Codex Hammer* (earlier *Codex Leicester*). In *The Notebooks of Leonardo da*
487 *Vinci* (ed. and trans. E. MacCurdy).. George Braziller.
- 488 DE GENNES, P. G. 1985 Wetting: statics and dynamics. *Rev. Mod. Phys.* **57**, 827–863.
- 489 DENG, X., MAMMEN, L., BUTT, H.-J. & VOLLMER, D. 2012 Candle soot as a template for a
490 transparent robust superamphiphobic coating. *Science* **335** (6064), 67–70.
- 491 DRISCOLL, M. M. & NAGEL, S. R. 2011 Ultrafast interference imaging of air in splashing
492 dynamics. *Phys. Rev. Lett.* **107** (15), 154502.
- 493 EGGLERS, J., FONTELOS, M. A., JOSSERAND, C. & ZALESKI, S. 2010 Drop dynamics after
494 impact on a solid wall: theory and simulations. *Phys. Fluids* **22** (6), 062101.
- 495 FUKAI, J., SHIIBA, Y., YAMAMOTO, T., MIYATAKE, O., POULIKAKOS, D., MEGARIDIS, C. M.
496 & ZHAO, Z. 1995 Wetting effects on the spreading of a liquid droplet colliding with a flat
497 surface: experiment and modeling. *Phys. Fluids* **7**, 236–247.
- 498 GARCÍA-GEIJO, P., RIBOUX, G. & GORDILLO, JM 2024 The skating of drops impacting over gas
499 or vapour layers. *J. Fluid Mech.* **980**, A35.
- 500 GAUTHIER, A., SYMON, S., CLANET, C. & QUÉRÉ, D. 2015 Water impacting on
501 superhydrophobic macrotextures. *Nat. Commun.* **6** (1), 1–6.
- 502 GOHARDANI, O. 2011 Impact of erosion testing aspects on current and future flight conditions.
503 *Prog. Aerosp. Sci.* **47** (4), 280–303.
- 504 GORDILLO, J. M., RIBOUX, G. & QUINTERO, E. S. 2019 A theory on the spreading of impacting
505 droplets. *J. Fluid Mech.* **866**, 298–315.
- 506 GORDILLO, L., SUN, T.-P. & CHENG, X. 2018 Dynamics of drop impact on solid surfaces:
507 evolution of impact force and self-similar spreading. *J. Fluid Mech.* **840**, 190–214.
- 508 GORIN, B., DI MAURO, G., BONN, D. & KELLAY, H. 2022 Universal aspects of droplet spreading
509 dynamics in Newtonian and non-Newtonian fluids. *Langmuir* **38** (8), 2608–2613.
- 510 HAO, C., LIU, Y., CHEN, X., LI, J., ZHANG, M., ZHAO, Y. & WANG, Z. 2016 Bioinspired
511 interfacial materials with enhanced drop mobility: from fundamentals to multifunctional
512 applications. *Small* **12** (14), 1825–1839.
- 513 HE, L., DING, L., LI, B., MU, W., LI, P. & LIU, F. 2021 Optimization strategy to
514 inhibit droplets rebound on pathogen-modified hydrophobic surfaces. *ACS Appl. Mater.*
515 *Interfaces* **13** (32), 38018–38028.
- 516 HOFFMAN, H., SIJS, R., DE GOEDE, T. & BONN, D. 2021 Controlling droplet deposition with
517 surfactants. *Phys. Rev. Fluids* **6** (3), 033601.
- 518 JHA, A., CHANTELOT, P., CLANET, C. & QUÉRÉ, D. 2020 Viscous bouncing. *Soft Matter* **16**,
519 7270–7273.
- 520 JI, B., YANG, Z. & FENG, J. 2021 Compound jetting from bubble bursting at an air-oil-water
521 interface. *Nat. Commun.* **12** (1), 6305.
- 522 JIN, P., ZHAO, K., BLIN, Z., ALLAIS, M., MOUTERDE, T. & QUÉRÉ, D. 2023 When marbles
523 challenge pearls. *J. Chem. Phys.* **158** (20).
- 524 JOSSERAND, C. & THORODDSEN, S. T. 2016 Drop impact on a solid surface. *Annu. Rev. Fluid*
525 *Mech.* **48**, 365–391.
- 526 JOWKAR, S. & MORAD, M. R. 2019 Rebounding suppression of droplet impact on hot surfaces:
527 effect of surface temperature and concaveness. *Soft Matter* **15** (5), 1017–1026.

- KIM, J. 2007 Spray cooling heat transfer: The state of the art. *Int. J. Heat Fluid Flow* **28** (4), 753–767.
- KIM, S., WU, Z., ESMALI, E., DOMBROSKIE, J. J & JUNG, S. 2020 How a raindrop gets shattered on biological surfaces. *Proc. Natl. Acad. Sci. U.S.A.* **117** (25), 13901–13907.
- KOLINSKI, J. M., MAHADEVAN, L. & RUBINSTEIN, S. M. 2014 Drops can bounce from perfectly hydrophilic surfaces. *Europhys. Lett.* **108**, 24001.
- KOOIJ, S., SIJS, R., DENN, M. M., VILLERMAUX, E. & BONN, D. 2018 What determines the drop size in sprays? *Phys. Rev. X* **8** (3), 031019.
- LAAN, N., DE BRUIN, K. G., BARTOLO, D., JOSSERAND, C. & BONN, D. 2014 Maximum diameter of impacting liquid droplets. *Phys. Rev. Appl.* **2** (4), 044018.
- LAFUMA, A. & QUÉRÉ, D. 2003 Superhydrophobic states. *Nat. Mater.* **2** (7), 457–460.
- LANGLEY, K., LI, E. Q. & THORODDSEN, S. T. 2017 Impact of ultra-viscous drops: air-film gliding and extreme wetting. *J. Fluid Mech.* **813**, 647–666.
- LESSER, M. B. 1981 Analytic solution of liquid-drop impact problems. *Proc. R. Soc. Lond. A* **377** (1770), 289–308.
- LI, J., ZHANG, B., GUO, P. & LV, Q. 2014 Impact force of a low speed water droplet colliding on a solid surface. *J. Appl. Phys.* **116** (21), 214903.
- LI, Y., QUÉRÉ, D., LV, C. & ZHENG, Q. 2017 Monostable superrepellent materials. *Proc. Natl. Acad. Sci. USA* **114** (13), 3387–3392.
- LIU, M., WANG, S. & JIANG, L. 2017 Nature-inspired superwettability systems. *Nat. Rev. Mater.* **2** (7), 17036.
- LOHSE, D. 2022 Fundamental fluid dynamics challenges in inkjet printing. *Annu. Rev. Fluid Mech.* **54**, 349–382.
- LOHSE, D. & VILLERMAUX, E. 2020 Double threshold behavior for breakup of liquid sheets. *Proc. Natl. Acad. Sci. U.S.A.* **117**, 18912–18914.
- MA, Y. & HUANG, H. 2023 Scaling maximum spreading of droplet impacting on flexible substrates. *J. Fluid Mech.* **958**, A35.
- MANDRE, S., MANI, M. & BRENNER, M. P. 2009 Precursors to splashing of liquid droplets on a solid surface. *Phys. Rev. Lett.* **102** (13), 134502.
- MARTOUZET, G., JØRGENSEN, L., PELET, Y., BIANCE, A.-L. & BARENTIN, C. 2021 Dynamic arrest during the spreading of a yield stress fluid drop. *Phys. Rev. Fluids* **6** (4), 044006.
- MIRELS, H. 1955 Laminar boundary layer behind shock advancing into stationary fluid. *NACA TN* **3401**, 25.
- MITCHELL, B. R., KLEWICKI, J. C., KORKOLIS, Y. P. & KINSEY, B. L. 2019 The transient force profile of low-speed droplet impact: measurements and model. *J. Fluid Mech.* **867**, 300–322.
- MOLÁČEK, J. & BUSH, J. W. M. 2012 A quasi-static model of drop impact. *Phys. Fluids* **24** (12), 127103.
- NEARING, M. A., BRADFORD, J. M. & HOLTZ, R. D. 1986 Measurement of force vs. time relations for waterdrop impact. *Soil Sci. Soc. Am. J.* **50**, 1532–1536.
- PAPADOPOULOS, P., MAMMEN, L., DENG, X., VOLLMER, D. & BUTT, H.-J. 2013 How superhydrophobicity breaks down. *Proc. Natl Acad. Sci. USA* **110** (9), 3254–3258.
- PHILIPPI, J., LAGRÉE, P.-Y. & ANTOKOWIAK, A. 2016 Drop impact on a solid surface: short-time self-similarity. *J. Fluid Mech.* **795**, 96–135.
- PÖHLKER, M. L., PÖHLKER, C., KRÜGER, O. O., FÖRSTER, J.-D., BERKEMEIER, T., ELBERT, W., FRÖHLICH-NOWOISKY, J., PÖSCHL, U., BAGHERI, G., BODENSCHATZ, E., HUFFMAN, J. A., SCHEITHAUER, S. & MIKHAILOV, E. 2023 Respiratory aerosols and droplets in the transmission of infectious diseases. *Rev. Mod. Phys.* **95** (4), 045001.
- POPINET, S. 2009 An accurate adaptive solver for surface-tension-driven interfacial flows. *J. Comput. Phys.* **228** (16), 5838–5866.
- POPINET, S. 2018 Numerical models of surface tension. *Annu. Rev. Fluid Mech.* **50**, 49–75.
- POPINET, S. & COLLABORATORS 2013–2023 Basilisk C: volume of fluid method. <http://basilisk.fr> (Last accessed: August 23, 2023).
- QUÉRÉ, D. 2008 Wetting and roughness. *Annu. Rev. Mater. Res.* **38**, 71–99.
- RAMÍREZ-SOTO, O., SANJAY, V., LOHSE, D., PHAM, J. T. & VOLLMER, D. 2020 Lifting a sessile drop from a superamphiphobic surface with an impacting one. *Sci. Adv.* **6**, eaba4330.

- REIN, M. 1993 Phenomena of liquid drop impact on solid and liquid surfaces. *Fluid Dyn. Res.* **12**, 61–93.
- RENARDY, Y., POPINET, S., DUCHEMIN, L., RENARDY, M., ZALESKI, S., JOSSERAND, C., DRUMRIGHT-CLARKE, M. A., RICHARD, D., CLANET, C. & QUÉRÉ, D. 2003 Pyramidal and toroidal water drops after impact on a solid surface. *J. Fluid Mech.* **484**, 69–83.
- RIBOUX, G. & GORDILLO, J. M. 2014 Experiments of drops impacting a smooth solid surface: a model of the critical impact speed for drop splashing. *Phys. Rev. Lett.* **113** (2), 024507.
- RICHARD, D., CLANET, C. & QUÉRÉ, D. 2002 Contact time of a bouncing drop. *Nature* **417** (6891), 811–811.
- RICHARD, D. & QUÉRÉ, D. 2000 Bouncing water drops. *Europhys. Lett.* **50** (6), 769–775.
- SANJAY, V. 2022 Viscous Free-Surface Flows. PhD thesis, University of Twente.
- SANJAY, V. 2023 VatsalSy/Impact-forces-of-water-drops-falling-on-superhydrophobic-surfaces: Impact Forces of Water Drops Falling on Superhydrophobic Surfaces. <https://doi.org/10.5281/zenodo.7598181>.
- SANJAY, V., CHANTELOT, P. & LOHSE, D. 2023a When does an impacting drop stop bouncing? *Journal of Fluid Mechanics* **958**, A26.
- SANJAY, V., LAKSHMAN, S., CHANTELOT, P., SNOEIJER, J. H. & LOHSE, D. 2023b Drop impact on viscous liquid films. *J. Fluid Mech.* **958**, A25.
- SANJAY, V. & LOHSE, D. 2024 The unifying theory of scaling in drop impact: forces & maximum spreading diameter. *In preparation*.
- SANJAY, V., LOHSE, D. & JALAAL, M. 2021 Bursting bubble in a viscoplastic medium. *J. Fluid Mech.* **922**, A2.
- SANJAY, V., SEN, U., KANT, P. & LOHSE, D. 2022 Taylor-Culick retractions and the influence of the surroundings. *J. Fluid Mech.* **948**, A14.
- SBRAGAGLIA, M., PETERS, A. M., PIRAT, C., BORKENT, B. M., LAMMERTINK, R. G. H., WESSLING, M. & LOHSE, D. 2007 Spontaneous breakdown of superhydrophobicity. *Phys. Rev. Lett.* **99** (15), 156001.
- SCHLICHTING, H. 1968 *Boundary-layer theory*. McGraw-Hill.
- SCHROLL, R. D., JOSSERAND, C., ZALESKI, S. & ZHANG, W. W. 2010 Impact of a viscous liquid drop. *Phys. Rev. Lett.* **104** (3), 034504.
- SHARMA, P. K. & DIXIT, H. N. 2021 Regimes of wettability-dependent and wettability-independent bouncing of a drop on a solid surface. *J. Fluid Mech.* **908**, A37.
- SHIRI, S. & BIRD, J. C. 2017 Heat exchange between a bouncing drop and a superhydrophobic substrate. *Proc. Natl. Acad. Sci. U.S.A.* **114** (27), 6930–6935.
- SIJS, R. & BONN, D. 2020 The effect of adjuvants on spray droplet size from hydraulic nozzles. *Pest. Manage. Sci.* **76** (10), 3487–3494.
- SMITH, F. R. & BRUTIN, D. 2018 Wetting and spreading of human blood: recent advances and applications. *Curr. Opin. Colloid Interface Sci.* **36**, 78–83.
- SMITH, F. R., NICLOUX, C. & BRUTIN, D. 2018 Influence of the impact energy on the pattern of blood drip stains. *Phys. Rev. Fluids* **3** (1), 013601.
- SMITH, M. I. & BERTOLA, V. 2010 Effect of polymer additives on the wetting of impacting droplets. *Phys. Rev. Lett.* **104**, 154502.
- SOTO, D., DE LARIVIERE, A. B., BOUTILLON, X., CLANET, C. & QUÉRÉ, D. 2014 The force of impacting rain. *Soft Matter* **10** (27), 4929–4934.
- SPRITTLES, JAMES E 2024 Gas microfilms in droplet dynamics: When do drops bounce? *Annu. Rev. Fluid Mech.* **56**, 91–118.
- THORAVAL, M.-J., SCHUBERT, J., KARPITSCHKA, S., CHANANA, M., BOYER, F., SANDOVAL-NAVAL, E., DIJKSMAN, J. F., SNOEIJER, J. H. & LOHSE, D. 2021 Nanoscopic interactions of colloidal particles can suppress millimetre drop splashing. *Soft Matter* **17** (20), 5116–5121.
- THORAVAL, M.-J., TAKEHARA, K., ETOH, T. G. & THORODDSEN, S. T. 2013 Drop impact entrapment of bubble rings. *J. Fluid Mech.* **724**, 234–258.
- TSAI, P., LAMMERTINK, R. G. H., WESSLING, M. & LOHSE, D. 2010 Evaporation-triggered wetting transition for water droplets upon hydrophobic microstructures. *Phys. Rev. Lett.* **104** (11), 116102.
- TUTEJA, A., CHOI, W., MA, M., MABRY, J. M., MAZZELLA, S. A., RUTLEDGE, G. C.,

- 640 MCKINLEY, G. H. & COHEN, R. E. 2007 Designing superoleophobic surfaces. *Science*
641 **318** (5856), 1618–1622.
- 642 VILLERMAUX, E. 2020 Fragmentation versus cohesion. *J. Fluid Mech.* **898**, P1.
- 643 VILLERMAUX, E. & BOSSA, B. 2011 Drop fragmentation on impact. *J. Fluid Mech.* **668**, 412–
644 435.
- 645 VILLERMAUX, E., WANG, X. & DEIKE, L. 2022 Bubbles spray aerosols: certitudes and mysteries.
646 *Proc. Natl. Acad. Sci. Nexus* **1** (5), pgac261.
- 647 VOLK, A. & KÄHLER, C. J. 2018 Density model for aqueous glycerol solutions. *Exp. Fluids*
648 **59** (5), 75.
- 649 WAGNER, H. 1932 Über Stoß- und Gleitvorgänge an der Oberfläche von Flüssigkeiten. *Z. Angew.*
650 *Math. Mech.* **12** (4), 193–215.
- 651 WILDEMAN, S., VISSER, C. W., SUN, C. & LOHSE, D. 2016 On the spreading of impacting
652 drops. *J. Fluid Mech.* **805**, 636–655.
- 653 WORTHINGTON, A. M. 1876a On the forms assumed by drops of liquids falling vertically on a
654 horizontal plate. *Proc. R. Soc.* **25** (171–178), 261–272.
- 655 WORTHINGTON, A. M. 1876b A second paper on the forms assumed by drops of liquids falling
656 vertically on a horizontal plate. *Proc. R. Soc.* **25** (171–178), 498–503.
- 657 WU, S., DU, Y., ALSAID, Y., WU, D., HUA, M., YAN, Y., YAO, B., MA, Y., ZHU, X. & HE,
658 X. 2020 Superhydrophobic photothermal icephobic surfaces based on candle soot. *Proc.*
659 *Natl Acad. Sci. USA* **117** (21), 11240–11246.
- 660 XU, L., ZHANG, W. W. & NAGEL, S. R. 2005 Drop splashing on a dry smooth surface. *Phys.*
661 *Rev. Lett.* **94** (18), 184505.
- 662 YARIN, A. L. 2006 Drop impact dynamics: splashing, spreading, receding, bouncing... *Annu.*
663 *Rev. Fluid Mech.* **38**, 159–192.
- 664 YARIN, A. L., ROISMAN, I. V. & TROPEA, C. 2017 *Collision Phenomena in Liquids and Solids*.
665 Cambridge University Press.
- 666 YUN, S. 2017 Bouncing of an ellipsoidal drop on a superhydrophobic surface. *Sci. Rep.* **7** (1),
667 17699.
- 668 ZHANG, B., LI, J., GUO, P. & LV, Q. 2017 Experimental studies on the effect of reynolds and
669 weber numbers on the impact forces of low-speed droplets colliding with a solid surface.
670 *Exp. Fluids* **58** (9), 1–12.
- 671 ZHANG, B., SANJAY, V., SHI, S., ZHAO, Y., LV, C. & LOHSE, D. 2022 Impact forces of water
672 drops falling on superhydrophobic surfaces. *Phys. Rev. Lett.* **129**, 104501.
- 673 ZHANG, R., ZHANG, B., LV, Q., LI, J. & GUO, P. 2019 Effects of droplet shape on impact
674 force of low-speed droplets colliding with solid surface. *Exp. Fluids* **60** (4), 64.
- 675 ZHENG, S., DILLAVOU, S. & KOLINSKI, J. M. 2021 Air mediates the impact of a compliant
676 hemisphere on a rigid smooth surface. *Soft Matter* **17** (14), 3813–3819.